**Pengcheng Wang[1]**
Department of Mechanical and
Aerospace Engineering,
Rutgers, The State University of New Jersey,
Piscataway, NJ 08854
e-mail: pengcheng.wang@rutgers.edu

**Feng Han**
Department of Mechanical and
Aerospace Engineering,
Rutgers, The State University of New Jersey,
Piscataway, NJ 08854
e-mail: fh233@rutgers.edu

**Jingang Yi[2]**
Fellow ASME
Department of Mechanical and Aerospace
Engineering,
Rutgers, The State University of New Jersey,
Piscataway, NJ 08854
e-mail: jgyi@rutgers.edu

# Gyroscopic Balancer-Enhanced Motion Control of an Autonomous Bikebot

*Bikebot (i.e., bicycle-based robot) is a class of underactuated balance robotic systems that require simultaneous trajectory tracking and balance control tasks. We present a tracking and balance control design of an autonomous bikebot. The external-internal convertible structure of the bikebot dynamics is used to design a causal feedback control to achieve both the tracking and balance tasks. A balance equilibrium manifold is used to define and capture the platform balance profiles and coupled interaction with the trajectory tracking performance. To achieve fully autonomous navigation, a gyrobalancer actuation is integrated with the steering and velocity control for stationary platform balance and stationary-moving switching. Stability and convergence analyses are presented to guarantee the control performance. Extensive experiments are presented to validate and demonstrate the autonomous control design. We also compare the autonomous control performance with human riding experiments and similar action strategies are found between them.* [DOI: 10.1115/1.4063014]

## 1 Introduction

Bicycle-based robot, here called bikebot, is a representative example of underactuated balance robot. Motion control of underactuated balance robots includes simultaneous trajectory tracking and platform balance. Considering planar motion, a bikebot has three degrees-of-freedom (DOFs), that is, the planar position and the roll motion of the body frame, while the available two control inputs include steering and velocity actuation. One major challenge of control of underactuated balance robots lies in the nonminimum phase, unstable internal subsystem, and its coupled dynamics with trajectory tracking of the external subsystem [1].

Modeling and control of single-track bikebots attracts extensive attention in past decades [2–6] and several autonomous bikebots have been developed [7–10]. With limited steering control capability, trajectory tracking and platform balancing are two competing tasks. To deal with the coupled dynamics, an external and internal convertible (EIC) structure of the bikebot dynamics was proposed in Refs. [4] and [6]. Under the EIC-based control, the target profiles of the internal subsystem are captured by the balance equilibrium manifold (BEM). The trajectory tracking control is first designed for the external subsystem, and the designed tracking control input is updated by enforcing the roll motion onto the BEM [11]. The work in Ref. [12] presented the calculation of the feasible motorcycle motion trajectory for aggressive, high-performance

maneuvers. The motorcycle dynamics models were used to estimate the maximum velocity profiles for high-performance maneuvers. In Refs. [13] and [14], dynamics model-based motion control was developed for motorcycle aggressive maneuvers. Tire-road interactions play an important role for the motion planning and velocity profile estimation for aggressive maneuvers.

When the bikebot stays stationary or moves at a low speed, the steering-induced balance torque is limited, and it becomes extremely difficult to balance the platform [15,16]. To assist the balance control, various actuation devices have been added and installed on the bicycle platform. Those devices include gyroscopic balancer [3,11,17], reaction wheel [9,18,19], inverted pendulum balancer [20,21], and movable counterweight [5,22], etc. Most of the above-mentioned control designs focus on the platform balance while the trajectory tracking is not among the main tasks. The work in Ref. [19] uses the interconnection and damping assignment passivity-based control method for an autonomous bikebot with an assistive flywheel. In Ref. [23], a backstepping technique and an optimal control method were used for the tracking and balance control of external and internal subsystems, respectively. Simulation results were included to demonstrate the autonomous bicycles.

In this paper, we present a motion and balance control systems design for the autonomous bikebot. The planar motion of the bikebot is built on the kinematics model (with the nonholonomic constraint), while the roll motion is based on the dynamics model. The focus of the control design covers both the bikebot navigation for given trajectories and stationary or low-speed balance tasks. For bikebot navigation, steering and velocity control is the main actuation, while at stationary, a gyrobalancer is primarily used to provide balance actuation. Instead of regulating roll motion to one (upright) position, we present an energy shaping-based orbital stabilization approach for stationary balance control using the gyrobalancer. The main

---

advantage of using the energy-shaping technique [24,25] lies in reduction of the magnitude of the needed gyroscopic balance torque and also relaxed gyrobalancer design constraints [17]. A coordination between the steering/velocity and gyrobalancer controls is also presented. The trajectory tracking control design is mainly built on the EIC structure of the bikebot dynamics and the stability and convergence analyses are presented. Extensive experiments are conducted to demonstrate the performance of the integrated control systems. Although the presented work mainly focuses on the autonomous bikebot, it is of interests to compare the motion control performance by the autonomous controller with the human rider control (e.g., Refs. [26] and [27]). Therefore, we include and discuss experimental comparison of the autonomous bikebot with the human riding performance.

The main contribution of this work lies in the extended EIC-based trajectory tracking and balance control of autonomous bikebots with experimental demonstration. To our best knowledge, few experimental demonstrations have been reported for the control of single-track mobile robots with only steering and velocity control. The experiments in Refs. [7] and [8] showed only the platform balance and trajectory tracking was not among the control tasks. The tracking experiments in Refs. [18–22] required assistive devices. Moreover, the comparison between the autonomous design and the rider control confirms similar strategies with the used BEM concept. The autonomous controller design of the bikebot navigation complements the human rider control strategies that were studied in Refs. [26–29]. Compared with the previous conference presentation [11,30,31], this work presents a more comprehensive design of bikebot system for both trajectory tracking and stationary balance control. We present a systemic way for stationary control and stationary-moving switching control. Convergence and stability are also guaranteed with additional experiments.

The rest of the paper is organized as follows. We present the bikebot-rider dynamics and introduce the EIC-based control in Sec. 2. Section 3 presents the gyrobalancer-enhanced tracking control, stationary balance, and stationary-to-moving switching. Experimental results and discussion are presented in Sec. 4. Finally, we summarize the concluding remarks in Sec. 5.

## 2 Bikebot-Rider Dynamics and Control

**2.1 System Dynamics.** Figure 1(a) shows the prototype of the autonomous bikebot, and Fig. 1(b) shows the human riding experiment setup. Although the main focus of this work is riderless bikebot control, we present a bikebot-rider dynamic model for human riding performance comparison purpose. Figure 1(c) shows the kinematic configuration of the bikebot and a rider's trunk. When human subjects riding the bikebot, their hands hold the handlebar, and the pitch motion of the human trunk is negligible. Therefore, we only consider the roll motion of the rider trunk.
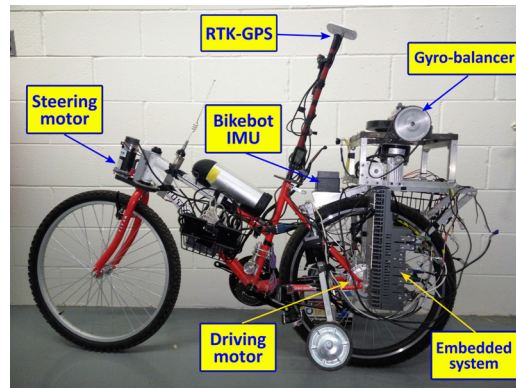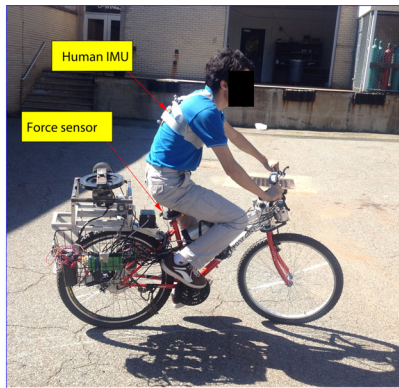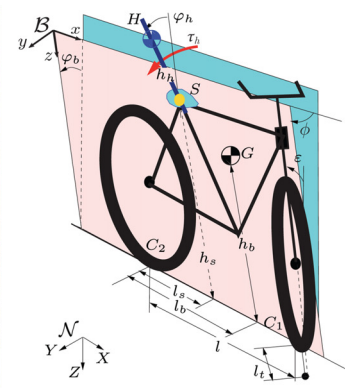
A ground-fixed frame $\mathcal{N}(X, Y, Z)$ (with the $Z$-axis downward) and a bikebot body frame $\mathcal{B}(x, y, z)$ are used. The roll and yaw angles of the bikebot are denoted as $\varphi_b$ and $\psi$, respectively. We denote the front and rear wheel contact points as $C_1$ and $C_2$, respectively. The origin of $\mathcal{B}$ is located at $C_2$, and frame $\mathcal{B}$ is obtained from $\mathcal{N}$ first by rotating around the $Z$-axis by $\psi$ and then by rotating around the $X$-axis by $\varphi_b$. The human trunk is modeled as a point mass $H$ on a massless rod that is pinned at seat position $S$. The distance from $H$ to $S$ is denoted as $h_h$, and the trunk roll angle is denoted as $\varphi_h$. The mass center $G$ of the bikebot and point $S$ are located at $[l_b \; 0 \; -h_b]^T$ and $[l_s \; 0 \; -h_s]^T$ in $\mathcal{B}$, respectively. The bikebot wheelbase length, caster angle, bikebot and human trunk mass are denoted as $l$, $\varepsilon$, $m_b$, and $m_h$, respectively. $l_t$ is the steering trail. The mass moment of inertia of the bikebot along the $x$-axis passing through $G$ is denoted as $J_b$.

The bikebot's planar motion is based on the kinematic model, and the bikebot-rider roll motion control is built on the dynamic model. Denoting the velocity of $C_2$ as $v_r$ and with the nonholonomic constraint at $C_2$, we calculate the yaw rate as [27]

$$\dot{\psi} = v_r \tan \phi \frac{c_\varepsilon}{l c_{\varphi_b}} \tag{1}$$

where $\phi$ is the steering angle and $c_\varepsilon = \cos \varepsilon (s_\varepsilon = \sin \varepsilon)$ for $\varepsilon$ and other angles. The ground is assumed to be flat and the pitch motion of the platform is neglected. Denoting the planar position of $C_2$ as $\boldsymbol{r}_{C_2} = [X \; Y]^T$ in $\mathcal{N}$, we obtain the kinematics model of the bikebot motion as

$$\boldsymbol{r}_{C_2}^{(3)} = \begin{bmatrix} X^{(3)} \\ Y^{(3)} \end{bmatrix} = \underbrace{\begin{bmatrix} c_\psi & -v_r s_\psi \\ s_\psi & v_r c_\psi \end{bmatrix}}_{\boldsymbol{R}_\psi} \begin{bmatrix} \ddot{v}_r \\ \ddot{\psi} \end{bmatrix} - \underbrace{\begin{bmatrix} v_r \dot{\psi} c_\psi + 2\dot{v}_r s_\psi \\ v_r \dot{\psi} s_\psi - 2\dot{v}_r c_\psi \end{bmatrix}}_{\boldsymbol{\Psi}} \dot{\psi}.$$

$$= \boldsymbol{R}_\psi \boldsymbol{u} - \boldsymbol{\Psi} \tag{2}$$

where $\boldsymbol{r}_{C_2}^{(m)}$ denotes the $m$-th order derivative of $\boldsymbol{r}_{C_2}$, $m \in \mathbb{N}$, and the same notation is used for other variables, input $\boldsymbol{u} = [u_r \; u_\psi]^T$, $u_r = \ddot{v}_r$ and $u_\psi = \ddot{\psi}$. The reason for taking the third derivative in Eq. (2) is to incorporate balance torque by the yaw angular acceleration.

Let $\boldsymbol{q} = [\varphi_b \; \varphi_h]^T$ and the equations of roll motion are obtained as [32]

$$\boldsymbol{M}(\boldsymbol{q})\ddot{\boldsymbol{q}} + \boldsymbol{C}(\boldsymbol{q}, \dot{\boldsymbol{q}}) + \boldsymbol{G}(\boldsymbol{q}) = \boldsymbol{\tau} + \boldsymbol{B}(\boldsymbol{q})\boldsymbol{u} \tag{3}$$

where $\boldsymbol{\tau} = [0 \; \tau_h]^T$ and $\tau_h$ is the torque that is applied by the rider along the roll motion direction; see Fig. 1(c). Matrices $\boldsymbol{M}(\boldsymbol{q})$, $\boldsymbol{C}(\boldsymbol{q}, \dot{\boldsymbol{q}})$, and $\boldsymbol{G}(\boldsymbol{q})$ denote the moment of inertia, Coriolis and gravitational effects, respectively. $\boldsymbol{B}(\boldsymbol{q})$ is the input matrix. The explicit form of these matrices are given in Eq. (4) on the top of the next page with $M_h = m_b h_b + m_h h_s$, $J_a = J_b + m_b h_b^2 + m_h(h_s^2 + h_h^2) + 2m_h h_s h_h c_{\varphi_h}$, $J_m = m_b h_b^2 + m_h h_s^2$, and $g = 9.8 \text{ m/s}^2$ is the gravitational constant.



Fig. 1  (a) The Rutgers bikebot system, (b) human riding experiments with wearable IMUs, and (c) a kinematic schematic of the bikebot-rider systems. The rider trunk is modeled as an inverted pendulum mounted at seat position S.

$$\boldsymbol{M}(\boldsymbol{q}) = \begin{bmatrix} J_a & m_h h_h (h_h + h_s c_{\varphi_h}) \\ m_h h_h (h_h + h_s c_{\varphi_h}) & m_h h_h^2 \end{bmatrix}, \quad \boldsymbol{C}(\boldsymbol{q}, \dot{\boldsymbol{q}}) = \begin{bmatrix} -m_h h_s h_h s_{\varphi_h}(2\dot{\varphi}_b + \dot{\varphi}_h)\dot{\varphi}_h - (J_m s_{\varphi_b} c_{\varphi_b} \\ + m_h h_h^2 s_{\varphi_b+\varphi_h} c_{\varphi_b+\varphi_h} + m_h h_s h_h s_{2\varphi_b+\varphi_h})\dot{\psi}^2 \\ + (M_h c_{\varphi_b} + m_h h_h c_{\varphi_h})v_r \dot{\psi} \\ \cdots\cdots\cdots\cdots\cdots\cdots\cdots\cdots\cdots\cdots \\ -m_h h_h h_s s_{\varphi_h}\dot{\varphi}_b\dot{\varphi}_h - m_h h_h(h_h s_{\varphi_h+\varphi_b} \\ + h_s s_{\varphi_h})c_{\varphi_h+\varphi_b}\dot{\psi}^2 + m_h h_h c_{\varphi_h}v_r\dot{\psi} \end{bmatrix},$$

$$\boldsymbol{G}(\boldsymbol{q}) = \begin{bmatrix} -M_h g s_{\varphi_b} - m_h h_h g s_{\varphi_b+\varphi_h} - (m_b l_b + m_h l_s)c_{\varphi_b} g l_t c_\varepsilon v_r^{-1}\dot{\psi} \\ -m_h g h_h s_{\varphi_b+\varphi_h} \end{bmatrix}, \quad \boldsymbol{B}(\boldsymbol{q}) = -\begin{bmatrix} 0 & m_b l_b h_b s_{\varphi_b} + m_h l_s h_s s_{\varphi_h} + m_h l_s h_h c_{\varphi_b+\varphi_h} \\ 0 & m_h h_h l_s c_{\varphi_h} \end{bmatrix} \quad (4)$$

Letting $\boldsymbol{u} = \boldsymbol{R}_\psi^{-1}(\boldsymbol{\Psi} + \boldsymbol{u}_N)$ and $\boldsymbol{u}_N \in \mathbb{R}^2$ as the controlled jerk, we rewrite Eqs. (2) and (3) into the following EIC form

$$\Sigma_{\text{ext}} : \boldsymbol{r}_{C_2}^{(3)} = \boldsymbol{u}_N \quad (5a)$$

$$\Sigma_{\text{int}} : \ddot{\boldsymbol{q}} = \boldsymbol{M}^{-1}(\boldsymbol{q})\Big[\boldsymbol{B}(\boldsymbol{q})\boldsymbol{R}_\psi^{-1}\boldsymbol{\Psi} - \boldsymbol{C}(\boldsymbol{q}, \dot{\boldsymbol{q}}) - \boldsymbol{G}(\boldsymbol{q}) \\ + \boldsymbol{\tau} + \boldsymbol{B}(\boldsymbol{q})\boldsymbol{R}_\psi^{-1}\boldsymbol{u}_N\Big] \quad (5b)$$

*Remark 1. The input $u_r = \ddot{v}_r$ is the controlled linear jerk (i.e., the derivative of acceleration $\dot{v}_r$). In experimental implementation, the designed input $u_r$ is integrated twice to obtain the velocity $v_r$ that is the control command for the driving motor. The other input $u_\psi = \ddot{\psi}$ is the controlled yaw acceleration of the bikebot. The input $u_\psi$ is first integrated to obtain the controlled yaw angular rate $\dot{\psi}$. Then, by relationship (1) between $\dot{\psi}$ and $\phi$, we obtain the controlled steering angle command $\phi = \tan^{-1}\left(\frac{\dot{\psi} l c_{\varphi_b}}{c_\varepsilon v_r}\right)$. Therefore, control input $\boldsymbol{u}$ is implemented by the driving and steering actuation in experiments.*

**2.2 Balance Equilibrium Manifold and Bikebot-Rider Control.** In this subsection, we present the tracking and balance control design using the EIC model by Eq. (5). Given the desired trajectory $\mathcal{T} : (X_d(t), Y_d(t))$ in $\mathcal{N}$, the first step is to design a tracking controller for $\Sigma_{\text{ext}}$ without considering the balance control task. Therefore, we consider

$$\boldsymbol{u}_N = \boldsymbol{u}_N^{\text{ext}} = \boldsymbol{r}_d^{(3)} - b_2 \ddot{\boldsymbol{e}}_p - b_1 \dot{\boldsymbol{e}}_p - b_0 \boldsymbol{e}_p \quad (6)$$

where $\boldsymbol{r}_d = [X_d(t)\ Y_d(t)]^T$ and $\boldsymbol{e}_p = \boldsymbol{r}_{C_2} - \boldsymbol{r}_d$. The constants $b_i > 0$, $i = 0, 1, 2$ are chosen such that polynomial $s^3 + b_2 s^2 + b_1 s + b_0$ is Hurwitz. By Eq. (6), the control input is designed as

$$\boldsymbol{u} = \boldsymbol{u}^{\text{ext}} = \boldsymbol{R}_\psi^{-1}\left(\boldsymbol{\Psi} + \boldsymbol{u}_N^{\text{ext}}\right) \quad (7)$$

Under Eq. (7), we define a nominal external vector field as

$$\boldsymbol{N}_{\text{ext}} = \begin{bmatrix} \dot{X} \\ \ddot{X} \\ X_d^{(3)} - \sum_{i=0}^{2} b_i e_X^{(i)} \\ \dot{Y} \\ \ddot{Y} \\ Y_d^{(3)} - \sum_{i=0}^{2} b_i e_Y^{(i)} \end{bmatrix} \quad (8)$$

We now consider the roll angle equilibrium, denoted as $\boldsymbol{q}_e$, by setting $\dot{\boldsymbol{q}} = \ddot{\boldsymbol{q}} = 0$ in Eq. (5b) under control (7). We define an implicit function of $\boldsymbol{q}$ as $\boldsymbol{F}(\boldsymbol{q}, \boldsymbol{u}, \boldsymbol{\tau}) = \boldsymbol{B}(\boldsymbol{q})\boldsymbol{u} + \boldsymbol{\tau} - \boldsymbol{C}(\boldsymbol{q}, \boldsymbol{0}) - \boldsymbol{G}(\boldsymbol{q})$ and let $\boldsymbol{q}_e = \boldsymbol{q}_e(\boldsymbol{u}, \boldsymbol{\tau})$ be the solution of the algebraic equation $\boldsymbol{F}(\boldsymbol{q}_e, \boldsymbol{u}, \boldsymbol{\tau}) = \boldsymbol{0}$ for given $\boldsymbol{u}$ and $\boldsymbol{\tau}$. The BEM under $\boldsymbol{u}^{\text{ext}}$ and $\boldsymbol{\tau}$, denoted by $\mathcal{E}(\boldsymbol{u}^{\text{ext}}, \boldsymbol{\tau})$, is defined as

$$\mathcal{E}(\boldsymbol{u}^{\text{ext}}, \boldsymbol{\tau}) = \left\{(\boldsymbol{x}, \alpha) \,|\, \boldsymbol{q} = \boldsymbol{q}_e(\boldsymbol{u}^{\text{ext}}, \boldsymbol{\tau}), \dot{\boldsymbol{q}} = \boldsymbol{0}\right\} \quad (9)$$

where $\boldsymbol{x} = \left[\boldsymbol{r}_{C_2}^T\ \dot{\boldsymbol{r}}_{C_2}^T\ \ddot{\boldsymbol{r}}_{C_2}^T\right]^T$ and $\alpha = \left[\boldsymbol{q}^T\ \dot{\boldsymbol{q}}^T\right]^T$. The BEM $\mathcal{E}(\boldsymbol{u}^{\text{ext}}, \boldsymbol{\tau})$ is viewed as a time-dependent graph of $\Sigma_{\text{ext}}$ that is evolved with $\boldsymbol{N}_{\text{ext}}$ under $\boldsymbol{u}^{\text{ext}}$ and $\boldsymbol{\tau}$. The value of $\boldsymbol{q}_e(\boldsymbol{u}^{\text{ext}}, \boldsymbol{\tau})$ in $\mathcal{E}(\boldsymbol{u}^{\text{ext}}, \boldsymbol{\tau})$ also depends on $\boldsymbol{x}$ implicitly through control $\boldsymbol{u}^{\text{ext}}$.

For internal subsystem by Eq. (5b), we need to stabilize the roll angle to $\boldsymbol{q}_e$. Noting $\boldsymbol{u} = [u_r\ u_\psi]^T$, we plug Eq. (7) into Eq. (5b) and obtain

$$\ddot{\boldsymbol{q}} = \boldsymbol{M}^{-1}(\boldsymbol{q})\left(\underbrace{\begin{bmatrix} B_{12}(\boldsymbol{q}) & 0 \\ B_{22}(\boldsymbol{q}) & 1 \end{bmatrix}}_{\boldsymbol{B}_\tau(\boldsymbol{q})}\overline{\boldsymbol{u}}^{\text{int}} - \boldsymbol{C}(\boldsymbol{q}, \dot{\boldsymbol{q}}) - \boldsymbol{G}(\boldsymbol{q})\right)$$

where $\overline{\boldsymbol{u}}^{\text{int}} = [u_\psi\ \tau_h]^T$ and $B_{ij}(\boldsymbol{q})$ is element of $\boldsymbol{B}(\boldsymbol{q})$ at the $i$th row and $j$th column, $i, j = 1, 2$. Note that $u_r$ does not appear in the above equation because the first column in $\boldsymbol{B}(\boldsymbol{q})$ is zero. From the above equation, the balance control of $\Sigma_{\text{int}}$ is

$$\overline{\boldsymbol{u}}^{\text{int}} = \boldsymbol{B}_\tau^{-1}(\boldsymbol{q})\left[\boldsymbol{C}(\boldsymbol{q}, \dot{\boldsymbol{q}}) + \boldsymbol{G}(\boldsymbol{q}) + \boldsymbol{M}(\boldsymbol{q})\boldsymbol{v}^{\text{int}}\right] \quad (10)$$

with $\boldsymbol{v}^{\text{int}} = \bar{L}_{N_{\text{ext}}}^2 \boldsymbol{q}_e - a_1 \dot{\boldsymbol{e}}_q - a_0 \boldsymbol{e}_q$, where constants $a_0, a_1 > 0$, $\boldsymbol{e}_q = \boldsymbol{q} - \boldsymbol{q}_e$, $\dot{\boldsymbol{e}}_q = \dot{\boldsymbol{q}} - \dot{\boldsymbol{q}}_e \approx \dot{\boldsymbol{q}} - \bar{L}_{N_{\text{ext}}}\boldsymbol{q}_e$. We approximate $\dot{\boldsymbol{q}}_e$ and $\ddot{\boldsymbol{q}}_e$ by using directional derivatives along $\boldsymbol{N}_{\text{ext}}$ due to their dependence on the external subsystems and $\boldsymbol{u}^{\text{ext}}$, i.e., $\bar{L}_{N_{\text{ext}}}\boldsymbol{q}_e = L_{N_{\text{ext}}}\boldsymbol{q}_e + \frac{\partial \boldsymbol{q}_e}{\partial t}$ and $\bar{L}_{N_{\text{ext}}}^2 \boldsymbol{q}_e = \bar{L}_{N_{\text{ext}}}\bar{L}_{N_{\text{ext}}}\boldsymbol{q}_e$. The form of $L_{N_{\text{ext}}}\boldsymbol{q}_e$ is,

$$\dot{\boldsymbol{q}}_e \approx \overline{L}_N \boldsymbol{q}_e = \left(\frac{\partial \boldsymbol{B}}{\partial \boldsymbol{q}_e}\boldsymbol{u}^{\text{ext}} - \frac{\partial(\boldsymbol{G} + \boldsymbol{C})}{\partial \boldsymbol{q}_e}\right)^{-1}\left(\boldsymbol{K} + \boldsymbol{B}\overline{L}_N \boldsymbol{u}^{\text{ext}}\right),$$

$$\overline{L}_N \boldsymbol{u}^{\text{ext}} = \frac{d}{dt}\left(\boldsymbol{R}_\psi^{-1}\boldsymbol{\Psi}\right) + \frac{d}{dt}\left(\boldsymbol{R}_\psi^{-1}\right)\boldsymbol{u}_N^{\text{ext}} + \boldsymbol{R}_\psi^{-1}L_N \boldsymbol{u}_N^{\text{ext}},$$

$$L_N \boldsymbol{u}_N^{\text{ext}} = \begin{bmatrix} X_d^{(4)} - b_0 \dot{e}_X - b_1 \ddot{e}_Y - b_2\left(u_{N,X}^{\text{ext}} - X_d^{(3)}\right) \\ Y_d^{(4)} - b_0 \dot{e}_Y - b_1 \ddot{e}_Y - b_2\left(u_{N,Y}^{\text{ext}} - Y_d^{(3)}\right) \end{bmatrix}$$

where $\boldsymbol{K}$ denotes a collection term of the derivative of $\boldsymbol{G}, \boldsymbol{C}, \boldsymbol{B}, \boldsymbol{\tau}$ with respective to variables other than $\boldsymbol{q}_e$, and $u_{N,X}$ and $u_{N,Y}$ denotes the components of control $\boldsymbol{u}_N^{\text{ext}}$ in $X$ and $Y$ dimension. The form of $\bar{L}_{N_{\text{ext}}}^2 \boldsymbol{q}_e$
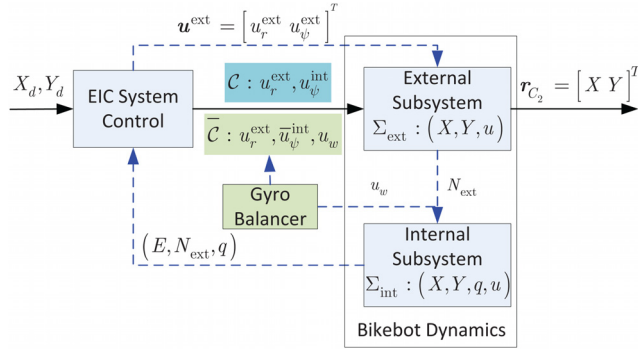
**Fig. 2 The flowchart of the EIC control scheme with gyrobalancer enhancement. The dashed line indicates the design flow and the solid line indicates the control flow.**

is obtained similarly. The overall control of the bikebot-rider system by Eq. (5) combines the controllers in Eqs. (7) and (10) as $u_r = u_r^{\text{ext}}$ and $u_\psi = u_\psi^{\text{int}}$, where $u_\psi^{\text{int}}$ is the first element of $\bar{\boldsymbol{u}}^{\text{int}}$ in Eq. (10).

*Remark 2. Although the above-developed control includes the human trunk motion and actuation, the design can be simplified for riderless autonomous control by reducing the roll motion and setting $\tau = 0$ in Eq. (5b). In the following section, we will use the above developments to present the riderless autonomous control to further illustrate the design.*

Figure 2 illustrates and summarizes the above EIC-based control scheme. For a given trajectory $\mathcal{T}$, the control system is first to specify the external systems controller $\boldsymbol{u}^{\text{ext}} = \begin{bmatrix} u_r^{\text{ext}} & u_\psi^{\text{ext}} \end{bmatrix}^T$ that is given by Eq. (7). Then, we compute the external vector field $N_{\text{ext}}$ by Eq. (8) and the BEM by Eq. (9). The final controller is updated by roll stabilization by Eq. (10) and given as $u_r = u_r^{\text{ext}}$ and $u_\psi = u_\psi^{\text{int}}$. In Sec. 3, we will discuss the gyrobalancer-enhanced control design.

# 3 Gyro-Balancer Enhanced Control

In this section, we mainly present the gyrobalancer control of bikebot and then discuss how to use the gyrobalancer to assist the stationary bikebot. Finally, the switching strategy between stationary balance and tracking control is briefly discussed.

## 3.1 Bikebot Model With the Gyro-Balancer.
Figure 3(a) illustrates the gyrobalancer configuration, and Fig. 3(b) shows the schematic of the riderless bikebot with the gyrobalancer. The gyrobalancer's flywheel rotates at high (constant) spinning speed



(a)        (b)
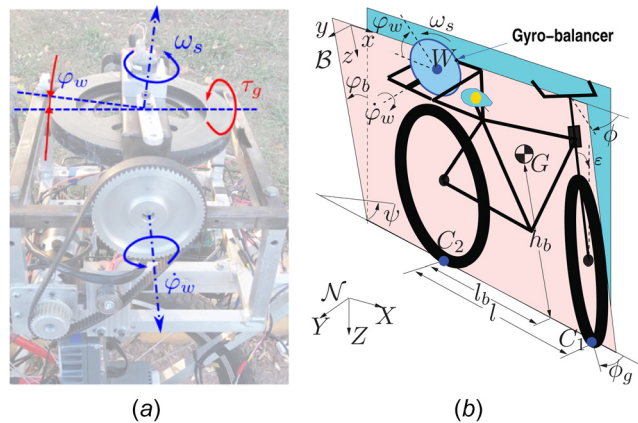
**Fig. 3 (a) The configuration of the gyrobalancer setup and (b) a kinematic schematic of the bikebot systems with the gyrobalancer**

$\omega_s$, and the flywheel's pivoting angle is denoted as $\varphi_w$. The gyroscopic torque along the roll motion is calculated as

$$\tau_g = -I_z c_{\varphi_w} \left( \omega_s - \frac{1}{2}\dot{\varphi}_b s_{\varphi_w} - \frac{1}{2}\dot{\psi} c_{\varphi_b} c_{\varphi_w} \right) \left( \dot{\varphi}_w + \dot{\psi} s_{\varphi_b} \right) \quad (11)$$

where $I_z$ is the mass moment of inertia of the flywheel about its rotating center.

To simplify the modeling process, the pivoting angular velocity is considered as the input $u_w = \dot{\varphi}_w$ and, similar to Eq. (3), the riderless roll dynamics model is obtained as

$$\Sigma_{\text{int}} : \ddot{\varphi}_b = J_t^{-1} \left[ f(\varphi_b) + g_\psi(\varphi_b)u_\psi + g_w u_w \right] \quad (12)$$

where $J_t = m_b h_b^2 + J_b + 0.5I_z \left( 1 + s_{\varphi_w}^2 \right)$, $g_\psi(\varphi_b) = -m_b h_b l_b c_{\varphi_b}$,

$$f(\varphi_b) = -m_b h_b c_{\varphi_b} v_r \dot{\psi} + m_b h_b^2 c_{\varphi_b} s_{\varphi_b} \dot{\psi}^2 + m_b h_b g s_{\varphi_b}$$
$$+ I_z c_{\varphi_w} c_{\varphi_b} \dot{\psi} \left( \omega_s - 0.5\dot{\varphi} s_{\varphi_w} - 0.5\dot{\psi} c_{\varphi_b} c_{\varphi_w} \right)$$
$$+ \frac{m_b g l_t l_b \tan\phi_\varepsilon c_{\varphi_b}}{l},$$
$$g_w(\varphi_b) = -I_z c_{\varphi_w} \left( \omega_s - 0.5\dot{\varphi}_b s_{\varphi_w} - 0.5\dot{\psi} c_{\varphi_b} c_{\varphi_w} \right)$$

Together with Eq. (5a), the above dynamics in Eq. (12) satisfies the EIC property.

## 3.2 Enhanced Tracking Control With the Gyro-Balancer.
We first consider the case that the gyrobalancer control is not used, that is, $u_w = 0$. The control design follows the discussion in Sec. 2.2. Under $\boldsymbol{u}^{\text{ext}}$ in Eq. (7), the balance equilibrium angle $\varphi_b^e$ in Eq. (9) satisfies the following relationship

$$f\left(\varphi_b^e\right) + g_\psi\left(\varphi_b^e\right)u_\psi^{\text{ext}} = 0 \quad (13)$$

From Eq. (10), the roll motion stabilization control is chosen as

$$u_\psi^{\text{int}} = g_\psi^{-1}(\varphi_b)\left(-f(\varphi_b) + J_t v_\psi^{\text{int}}\right) \quad (14)$$

with $v^{\text{int}} = \bar{L}_{N_{\text{ext}}}^2 \varphi_b^e - a_1 \dot{e}_{\varphi_b} - a_0 e_{\varphi_b}$, where $e_b = \varphi_b - \varphi_b^e$, $\dot{e}_{\varphi_b} = \dot{\varphi}_b - \dot{\varphi}_b^e \approx \dot{\varphi}_b - \bar{L}_{N_{\text{ext}}}\varphi_b^e$, and constants $a_0, a_1 > 0$. The overall control design combines Eqs. (7) and (14) as

$$\mathcal{C} : u_r = u_r^{\text{ext}}, \ u_\psi = u_\psi^{\text{int}}, u_w = 0 \quad (15)$$

*Remark 3. Under controller $\mathcal{C}$ in Eq. (15), both the position tracking error $\boldsymbol{e}_p$ and roll motion error $e_{\varphi_b}$ are shown to exponentially converge to neighborhoods around zero simultaneously. The stability and convergence proofs are obtained by using the EIC properties and a technical assumption about the BEM approximation error in the closed-loop dynamics [4]. A similar proof is given in Ref. [26] and we omit here.*

We now derive the gyrobalancer control $u_w$ and steering control $\bar{u}_\psi^{\text{int}}$ to further improve the trajectory tracking performance. By the EIC-based design, under $\boldsymbol{u}^{\text{ext}}$, the bikebot position converges to the desired trajectory $\mathcal{T}$ exponentially. For the balance task, the steering input $u_\psi^{\text{int}}$ is different from $u_\psi^{\text{ext}}$ and thus introduces tracking errors $\boldsymbol{e}_p$. On the other hand, $u_\psi^{\text{int}}$ has to drive $\varphi_b$ to $\varphi_b^e$. The goal of the gyrobalancer control $u_w$ is to help balance the platform under $\bar{u}_\psi^{\text{int}}$. Under $u_w$ and $\bar{u}_\psi^{\text{int}}$, the balancing capability is assumed to be the same as $u_\psi^{\text{int}}$ with $u_w = 0$, namely, the right-hand sides of Eq. (12) are the same and thus, we obtain

$$f(\varphi_b) + g_\psi(\varphi_b)u_\psi^{\text{int}} = f(\varphi_b) + g_\psi(\varphi_b)\bar{u}_\psi^{\text{int}} + g_w(\varphi_b)u_w \quad (16)$$

Downloaded from http://asmedigitalcollection.asme.org/dynamicsystems/article-pdf/145/10/101002/7035810/ds_145_10_101002.pdf by Rutgers University, Jingang Yi on 12 December 2023

If the external control by Eq. (6) is used, we have

$$r_d^{(3)} - b_2\ddot{e}_p - b_1\dot{e}_p - b_0 e_p = \mathbf{\Psi} + \mathbf{R}_\psi \mathbf{u}^{\text{ext}}$$

By inputs Eqs. (14) and (15), the actual planar motion is then $\mathbf{r}_{C_2}^{(3)} = \mathbf{\Psi} + \mathbf{R}_\psi \overline{\mathbf{u}}, \overline{\mathbf{u}} = \left[ u_r^{\text{ext}} \ u_\psi^{\text{int}} \right]^T$. The tracking error due to the balance control is

$$e_p^{(3)} + b_2\ddot{e}_p + b_1\dot{e}_p + b_0 e_p = \mathbf{d}_p := \mathbf{R}_\psi \begin{bmatrix} 0 \\ u_\psi^{\text{int}} - u_\psi^{\text{ext}} \end{bmatrix} \quad (17)$$

Using Eq. (13), we obtain an alternative formulation for $u_\psi^{\text{ext}}$ as

$$u_\psi^{\text{ext}} = -g_\psi^{-1}(\varphi_b^e) f(\varphi_b^e) \quad (18)$$

Substituting $u_\psi^{\text{int}}$ in and $u_\psi^{\text{ext}}$ in Eqs. (18) into (17), we obtain the error perturbation term $\mathbf{d}_p$ as

$$\mathbf{d}_p = \mathbf{R}_\psi \begin{bmatrix} 0 \\ d_0 \end{bmatrix} \quad (19)$$

where $d_0 = u_\psi^{\text{int}} - u_\psi^{\text{ext}} = -g_\psi^{-1}(\varphi_b)f(\varphi_b) + g_\psi^{-1}(\varphi_b^e)f(\varphi_b^e) + g_\psi^{-1}(\varphi_b)J_t v_\psi^{\text{int}}$. Under the new control $\overline{u}_\psi^{\text{int}}$, we obtain a similar error perturbation $\overline{\mathbf{d}}_p$ as

$$\overline{\mathbf{d}}_p = \mathbf{R}_\psi \begin{bmatrix} 0 \\ \overline{d}_0 \end{bmatrix} = \mathbf{R}_\psi \begin{bmatrix} 0 \\ \overline{u}_\psi^{\text{int}} - u_\psi^{\text{ext}} \end{bmatrix} \quad (20)$$

where $\overline{d}_0 = -g_\psi^{-1}(\varphi_b)f(\varphi_b) + g_\psi^{-1}(\varphi_b^e)f(\varphi_b^e) + g_\psi^{-1}(\varphi_b)J_t v_\psi^{\text{int}} - g_\psi^{-1}(\varphi_b)g_w(\varphi_b)u_w$. From Eq. (20), if $\overline{u}_\psi^{\text{int}} = u_\psi^{\text{ext}}$, then $\overline{\mathbf{d}}_p = \mathbf{0}$ and errors $e_p$ converge by Eq. (17). However, given Eq. (16) and the restrictive pivoting motion, the magnitude of $\overline{u}_\psi^{\text{int}}$ cannot be arbitrarily chosen.

We design $u_w$ and $\overline{u}_\psi^{\text{int}}$ by considering the physical constraints of the gyrobalancer actuation, namely,

$$|\varphi_w| \leq \varphi_w^{\max}, |\dot{\varphi}_w| \leq u_w^{\max}, |\ddot{\varphi}_w| \leq \gamma_w^{\max} \quad (21)$$

where $\varphi_w^{\max}$, $u_w^{\max}$, and $\gamma_w^{\max}$ are, respectively, the maximum pivoting angle, angular velocity, and angular acceleration. By these constraints, we define the upper- and lower-bound functions for $u_w$, that is, $f_{wc}^-(\varphi_w) \leq u_w \leq f_{wc}^+(\varphi_w)$, where

$$f_{wc}^+(\varphi_w) = \begin{cases} u_w^{\max}, & -\varphi_w^{\max} \leq \varphi_w \leq \varphi_{w1} \\ 2\gamma_w^{\max}\sqrt{\varphi_w^{\max} - \varphi_w}, & \varphi_{w1} < \varphi_w \leq \varphi_w^{\max} \end{cases}$$

$$f_{wc}^-(\varphi_w) = -f_{wc}^+(-\varphi_w), \ \varphi_{w1} = \varphi_w^{\max} - \frac{(u_w^{\max})^2}{2\gamma_w^{\max}}$$

The above bounds are calculated by the pivoting motion kinematics with the constraints in Eq. (21). If $|d_0| > \varepsilon_d$ for a given $\varepsilon_d > 0$, we design the rolling torque in the direction of $g_\psi(\varphi_b)\left( u_\psi^{\text{int}} - u_\psi^{\text{ext}} \right)$ and given constraints $f_{wc}^+(\varphi_w)$ and $f_{wc}^-(\varphi_w)$, that is,

$$u_w^0 = \text{sign}(u_w) \min\left( |g_w^{-1}(\varphi_b)g_\psi(\varphi_b)(|d_0| - \varepsilon_d)|, |f_{wc}^\pm(\varphi_w)| \right) \quad (22)$$

where $\text{sign}(u_w) = \text{sign}\left( g_w^{-1}(\varphi_b)g_\psi(\varphi_b)d_0 \right)$. If $|d_0| \leq \varepsilon_d$, we choose $u_w^0 = 0$. From Eq. (16), the steering control $\overline{u}_\psi^{\text{int}}$ is

$$\overline{u}_\psi^{\text{int}} = g_\psi^{-1}(\varphi_b)\left[ J_t v_\psi^{\text{int}} - f(\varphi_b) - g_w(\varphi_b)u_w^0 \right] \quad (23)$$

The overall control with gyrobalancer assistance is then

$$\overline{\mathcal{C}} : u_r = u_r^{\text{ext}}, u_\psi = \overline{u}_\psi^{\text{int}}, u_w = u_w^0 \quad (24)$$

Under controllers $\mathcal{C}$ in Eq. (15) and $\overline{\mathcal{C}}$ in Eq. (24), the position tracking errors are denoted as $e_p$ and $\overline{e}_p$, respectively. It can be shown that under $\overline{\mathcal{C}}$, the magnitude of the tracking errors is reduced. We first present the following result.

LEMMA 1. *The error disturbance $\overline{\mathbf{d}}_p$ under controller $\overline{\mathcal{C}}$ is not greater than that of $\mathbf{d}_p$ under controller $\mathcal{C}$.*

*Proof*. See Appendix A. ∎

Under $\overline{\mathcal{C}}$, the EIC structure is still held, and thus, as shown in Refs. [4] and [26], the closed-loop errors $e_p$ and $\overline{e}_p$ asymptotically converge to bounded regions near the origin. Similar to Eq. (17), we obtain the error dynamics for $\overline{e}_p$ as

$$\overline{e}_p^{(3)} + b_2\ddot{\overline{e}}_p + b_1\dot{\overline{e}}_p + b_0\overline{e}_p = \overline{\mathbf{d}}_p \quad (25)$$

Defining $\mathbf{e}_x = \left[ e_p^T \ \dot{e}_p^T \ \ddot{e}_p^T \right]^T$ and $\overline{\mathbf{e}}_x = \left[ \overline{e}_p^T \ \dot{\overline{e}}_p^T \ \ddot{\overline{e}}_p^T \right]^T$, similar to Ref. [26], we obtain that the magnitudes of $\mathbf{d}_p$ and $\overline{\mathbf{d}}_p$ are assumed to be affine functions of $\mathbf{e}_x$ and $\overline{\mathbf{e}}_x$, respectively,

$$||\mathbf{d}_p|| \leq k_0 + k_1||\mathbf{e}_x||, \ ||\overline{\mathbf{d}}_p|| \leq \overline{k}_0 + \overline{k}_1||\overline{\mathbf{e}}_x|| \quad (26)$$

where $k_0, k_1, \overline{k}_0, \overline{k}_1 > 0$ are constants. Given the result in Lemma 1, we assume that $\overline{k}_0 \leq k_0, \overline{k}_1 \leq k_1$. We have the following results about errors $e_p$ and $\overline{e}_p$.

THEOREM 1. *Under controllers $\mathcal{C}$ and $\overline{\mathcal{C}}$, $e_p(t)$ and $\overline{e}_p(t)$ exponentially converge to regions near the origin. Moreover, denoting the error bounds $e_p^b(t)$ and $\overline{e}_p^b(t)$, i.e., $||e_p(t)|| \leq e_p^b(t)$ and $||\overline{e}_p(t)|| \leq \overline{e}_p^b(t)$, we obtain $\overline{e}_p^b(t) \leq e_p^b(t)$ for $t \geq 0$.*

*Proof*. See Appendix B. ∎

From Eq. (16), under $\overline{\mathcal{C}}$ the balancing control effect is the same as that of $\mathcal{C}$. The closed-loop error dynamics of $\Sigma_{\text{int}}$ is

$$\ddot{e}_{\varphi_b} + a_1\dot{e}_{\varphi_b} + a_0 e_{\varphi_b} = d_{\varphi_b} \quad (27)$$

where $d_{\varphi_b} = \ddot{\varphi}_b^e - \overline{L}_{N_{\text{ext}}}^2 \varphi_b^e + a_1\left( \dot{\varphi}_b^e - \overline{L}_{N_{\text{ext}}}\varphi_b^e \right)$, which is bounded by the norms of the desired trajectory [4]. Because of the unchanged internal error dynamics by Eq. (27) under $\mathcal{C}$ and $\overline{\mathcal{C}}$, the stability and tracking performance for the BEM is the same.

## 3.3 Stationary Balance With Gyro-Balancer Control.

When the bikebot is stationary, $v_r = 0$ and $u_\psi = 0$ and we consider balancing the bikebot by using the gyrobalancer. One constraint of the gyrobalancer is the lack of continuously supplied, large balance torque due to its working principle, that is, a constant pivoting rate $u_w$ is needed but an increased pivoting angle would reduce the output torque. Therefore, instead of regulating the roll angle at the upright position, we stabilize the platform at a designed orbit to further help avoid saturation of the output balance torque. We define the state variables as $\boldsymbol{\xi} = [\xi_1 \ \xi_2 \ \xi_3]^T = [\varphi_b \ \dot{\varphi}_b \ s_{\varphi_w}]^T$. From Eq. (12), the roll motion dynamics reduces to

$$\dot{\xi}_1 = \xi_2, \ \dot{\xi}_2 = f_g(\boldsymbol{\xi}) + g_g(\boldsymbol{\xi})u_g, \ \dot{\xi}_3 = u_g \quad (28)$$

where $u_g = c_{\varphi_w}u_w, f_g(\boldsymbol{\xi}) = \frac{m_b g h_b s_{\xi_1}}{J_t}, g_g(\boldsymbol{\xi}) = \frac{-I_z\omega_s + I_s\xi_2\xi_3}{J_t}$. The equilibrium of Eq. (28) is $\boldsymbol{\xi}_e = \mathbf{0}$ under $u_g = 0$. Given $I_z \ll J_b \ll m_b h_b^2$ and $|\xi_2| \ll \omega_s$, Eq. (28) is simplified to

$$\dot{\xi}_2 - \frac{g}{h_b}s_{\xi_1} + \frac{I_z\omega_s}{m_b h_b^2}u_g = 0 \quad (29)$$

We plan to stabilize the motion governed by Eq. (29) on an oscillation orbit $\mathcal{O}_b$ given by

$$\mathcal{O}_b : \dot{\xi}_2 + \frac{b}{h_b}s_{\xi_1} = 0 \quad (30)$$

where $b > 0$ is constant. Plugging Eqs. (30) into (29), we have $\dot{\xi}_3 = -\frac{(b+g)m_b h_b^2}{I_z\omega_s b}\dot{\xi}_2 = -L\dot{\xi}_2$, where $L = \frac{(g+b)m_b h_b^2}{I_z b\omega_s}$. The corresponding orbital trajectory for $\xi_3$ is given by $\mathcal{O}_g : \xi_3 = -L\xi_2$.

We consider an energy-like function $E(\xi) = \frac{1}{2}m_b h_b^2 \xi_2^2 + m_b h_b b (1 - c_{\xi_1})$. The maximum angle $\xi_1^*$ on orbit $\mathcal{O}_b$ is obtained at $\xi_2 = 0$. By Eq. (30), if $(\xi_1, \xi_2)$ is on $\mathcal{O}_b$, $E(\xi)$ is conserved at $E_d = m_b h_b b (1 - c_{\xi_1^*})$. Therefore, define $\Delta E = E(\xi) - E_d$ and the control law is given as

$$u_g = \frac{Lb}{h_b}\left(s_{\xi_1} + \kappa_2 v_g(\xi)\right), \quad v_g(\xi) = \xi_2 \Delta E + \gamma \kappa_1 (\xi_3 + L\xi_2) \quad (31)$$

where $\gamma = \frac{g}{bL\omega_s} > 0$, and $\kappa_1, \kappa_2 > 0$. We have the following result.

LEMMA 2. *Under control (31), the system by Eq. (28) converges to the invariant set $\mathcal{S}(\xi) = \{\xi | v_g(\xi) = 0\}$ asymptotically, and the closed-loop trajectories of $\xi$ are on orbits $\mathcal{O}_b$ and $\mathcal{O}_g$ simultaneously.*

*Proof.* See Appendix C. ∎

**3.4 Stationary-Moving Control Switch Strategy.** Noting that $|\dot{\varphi}_b| \ll \omega_s$ and $|I_x \dot{\varphi}_b s_{\varphi_w}| \ll I_z \omega_s$, the gyroscopic balance torque (11) is simplified as $\tau_g = -I_z \omega_s u_g$. The maximum instantaneous gyroscopic balance torque is then estimated as $\tau_g^{max} = I_z \omega_s u_w^{max}$. We compare the above gyroscopic balance torque with the steering-induced balance torque. Using the condition $\varphi_b \approx 0$ and at constant $\phi$, we simplify Eq. (12) and collect all terms related with the steering angle. The steering-induced balance torque is $\tau_s = m_b h_b c_{\varphi_b} v_r \dot{\psi} - \frac{m_b g l_t l_b \tan\phi c_s c_{\varphi_b}}{l} = m_b \frac{c_s}{l} \tan\phi (h_b v_r^2 - g l_t l_b)$. It is clear that with increasing steering angle $\phi$ and velocity $v_r$, $\tau_s$ value grows. It is however difficult to analyze and directly compare the magnitudes of $\tau_s$ and $\tau_g$ from the above calculations. We here illustrate the comparison numerically. Using the bikebot prototype parameters, Fig. 4 illustrates the balance torque $\tau_s$ as varying velocity and steering angle. When velocity $v_r$ is small, the value of $\tau_s$ is small. In this case, it is extremely challenging to only use steering actuation to balance the platform.

From the above discussion, for the stationary platform or at low-velocity motion, the bikebot balance is maintained by the gyrobalancer control only, while at large velocity, steering control is mainly used. Therefore, a switching strategy is needed between the gyrobalancer and steering controls. Stability under the switched control follows the design that the state under the current controller is within the region of attraction of the switched target controller. By
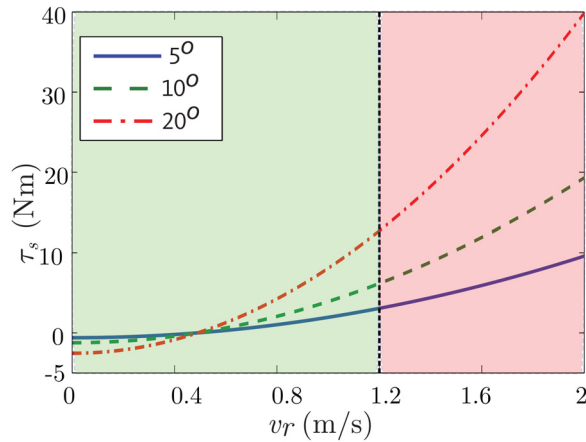
doing so, the stability of the switched control is guaranteed. For simplicity, velocity magnitude is chosen as the switching condition. The controlled torque is $\tau_\psi = g_\psi(\varphi_b)u$ $u_\psi = \frac{m h_b l_b c_\varepsilon}{l}[v_r(\sec_\phi^2 \dot{\phi} + \dot{\varphi}_b \tan\phi \tan\varphi_b) + \dot{v}_r \tan\phi]$. Clearly, to achieve effective steering control, the velocity needs to reach a certain value $v_1^*$, at which the bikebot roll motion state is within the region of attraction of the steering control. Similarly, when switching back to stationary balance control the by gyrobalancer, the effective design is to reduce the velocity below $v_2^*$ at which the steering effect is negligible and the gyrobalancer can safely take over the balance task to stop the bikebot.

# 4 Experimental Results

**4.1 Experimental System.** The bikebot prototype shown in Fig. 1(a) was modified from a mountain bicycle with a set of sensors and actuators. A high-resolution inertial measurement unit (IMU) (model 801; Motion Sense, Inc.) was used to obtain the roll angle $\varphi_b$ and yaw angle $\psi$ and their rates. Optical encoders were used to measure the velocity (from the rear wheel) and steering angle. A real-time kinematic (RTK) GPS unit (Novatel, Inc.) was used to obtain the bikebot position. The gyrobalancer was mounted on the rear rack. The flywheel and pivoting motion were each driven by a DC motor with encoders for feedback control; see Fig. 3(a). The steering actuation was driven by a DC motor (with an encoder for position feedback) and the bikebot velocity was driven by the hub motor at the rear wheel. A real-time embedded system (cRIO model 9082; National Instruments, Inc.) was used to collect all measurements and compute the control inputs at a frequency of 100 Hz. The positioning information from the GPS unit was updated at around 20 Hz. Table 1 lists the values of the physical parameters of the bikebot system. The following control gains and parameters were used in implementation: $a_0 = 25$, $a_1 = 180$, $b_0 = 3$, $b_1 = 6$, $b_2 = 10$ for the EIC controller; $b = 1$ for the orbital stabilization controller. The gyrobalancer physical constraints were given as: $\varphi_w^{max} = \frac{\pi}{2}$ rad, $u_w^{max} = 6$ rad/s, $\varepsilon_d = 2$ rad/s$^2$, and $\gamma_w^{max} = 6$ rad/s$^2$.

We conducted human-riding experiments to compare with the autonomous control. As shown in Fig. 1(b), the rider operated the bikebot similar to a regular bicycle with manual steering and regulating the velocity. Trajectory lines were marked on the ground so that the human subjects rode the bikebot to follow the trajectory as closely as possible. A 6DOF force/torque sensor (JR3, Inc.) was installed underneath the bikebot seat to obtain the rider's trunk torque $\tau_h$. An IMU (model 605; Motion Sense, Inc.) was mounted on the human trunk to obtain the rider trunk roll angle. The embedded system was used to collect and store the motion data at a frequency of 100 Hz. The subjects were experienced bicycle riders, and they rode the bikebot for about 10 min before experiments were recorded. An informed consent form was signed by human subjects and the testing protocol was approved by the Institutional Review Board (IRB) at Rutgers University.

**4.2 Experimental Results.** We first present the validation results for the bikebot-rider model by Eq. (3) using human riding experiments. Figure 5(a) shows the trajectory of the bikebot following an "8"-shape trajectory (with a radius of 3 m). The subject rodes the bikebot with a velocity of around 2 to 2.5 m/s. Figure 5(b) illustrates the validation of the two equations in Eq. (3). The plots compare the calculations of term $G(q)$, and the rest of the other terms in the dynamics equation is neglected. We chose this comparison method because the magnitude of $G(q)$ dominates the values of other terms. These results clearly show a close match



**Fig. 4 Steering-induced balance torque $\tau_s$ as function of velocity $v_r$ for the bikebot prototype model under different steering angles $\phi = 5, 10,$ and 20 deg**

**Table 1 The values of the bikebot physical parameters**

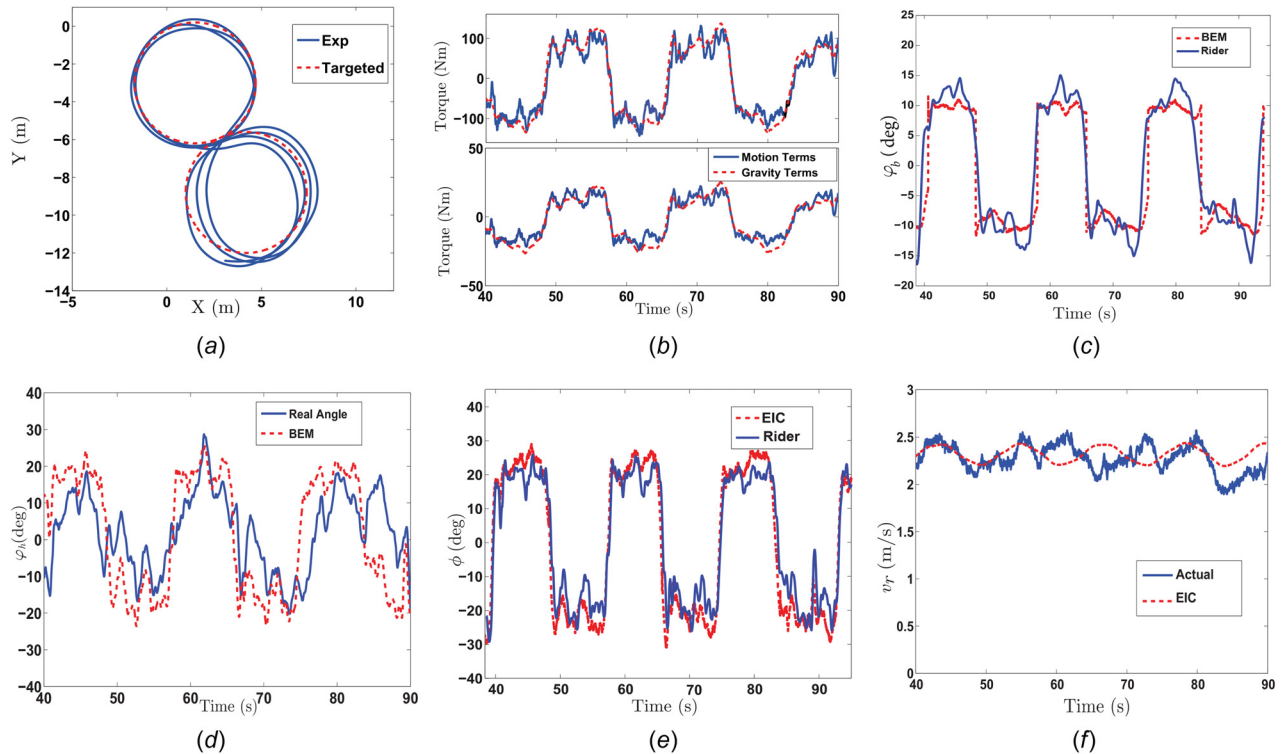| $m_b$ (kg) | $m_h$ (kg) | $J_b$ (kg m$^2$) | $I_z$ (kg m$^2$) | $h_h$ (m) | $h_b$ (m) | $l_b$ (m) | $h_s$ (m) | $l_s$ (m) | $l$ (m) | $l_t$ (m) | $\varepsilon$ (deg) | $\omega_s$ (rpm) |
|---|---|---|---|---|---|---|---|---|---|---|---|---|
| 51 | 35 | 2.5 | 0.036 | 0.30 | 0.64 | 0.27 | 0.85 | 0.32 | 1.1 | 0.06 | 20 | 1500 |

Fig. 5 (*a*) Human riding experiments trajectory of following an "8"-shape trajectory (radius of 6 m). (*b*) Validation of the bikebot-rider dynamics model in Eq. (3). The top plot shows the comparison of the first equation and the bottom plot is for the second equation in Eq. (3). (*c*) Bikebot roll angle $\varphi_b$ and the calculated BEM for $\varphi_b$. (*d*) Rider trunk roll angle $\varphi_h$ and the calculated BEM for $\varphi_h$. (*e*) Rider-controlled steering angle $\phi$ and EIC-based controlled $\phi$. (*f*) Rider-controlled bikebot velocity $v_r$ and EIC-based $v_r$. These plots were previously presented in Ref. [26].

between the model prediction and the experiments. Figures 5(*c*) and 5(*d*) show the bikebot and rider trunk roll angles, respectively. Using the steering angle, human trunk driving torque, and velocity measurements, we computed and plotted the BEM (i.e., $\varphi_h^e$ and $\varphi_b^e$). The actual angles followed closely with these equilibria. We also computed the EIC-based control design, and Figs. 5(*e*) and 5(*f*) show these control inputs (i.e., steering angle $\phi$ and velocity $v_r$)

together with the actual human inputs. The velocities labeled "EIC" in Figs. 5(*e*) and 5(*f*) were calculated using the system model, and the difference with the rider experiments is due to the modeling errors and variations of human riding behavior.

To demonstrate the influence of the moving velocity on trajectory tracking performance, we ran experiments by first regulating velocity $v_r$ at a constant value and using only the steering control.
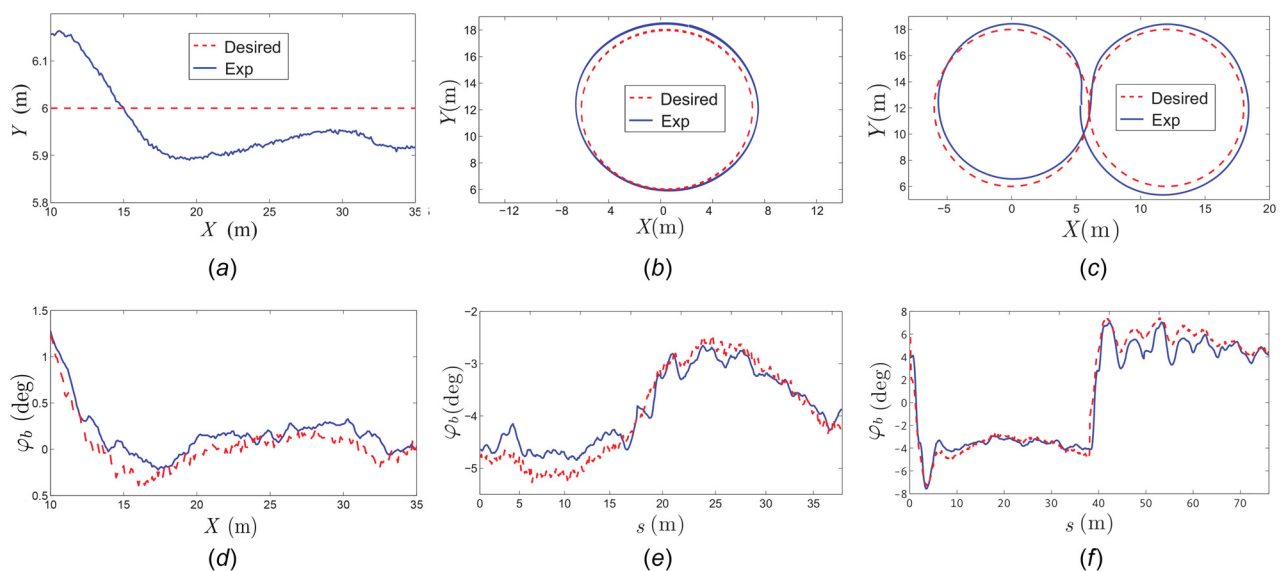


Fig. 6 Bikebot path following results with desired trajectories. Planar positions for (*a*) straight-line, (*b*) circular, and (*c*) "8"-shape trajectories. Bikebot roll angle results for the (*d*) straight-line, (*e*) circular, and (*f*) "8"-shape trajectories. The dashed curves in (*d*)–(*f*) represent the calculated BEM values.
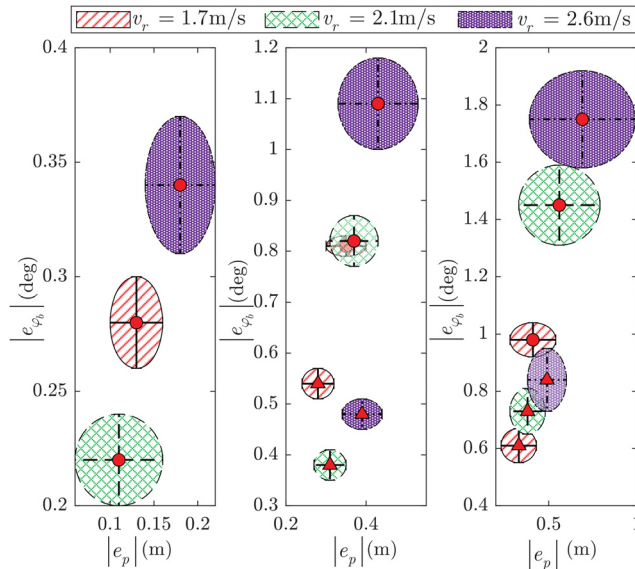
**Fig. 7 Bikebot path tracking error distributions (mean values as the centers and one standard deviation value as the major and minor axes of each ellipse). Left: straight-line tracking; middle: circular tracking; and Right: "8"-shape trajectory tracking. In the middle and right subfigures, the "▲" markers at the center indicate the 6-m radius trajectory and circular "•" markers for 4-m radius trajectory.**

Five sets of experiments were conducted: the straight-line, circular, and "8"-shape trajectories (radii 4 and 6 m) under velocity $v_r = 1.7, 2.1$, and 2.6 m/s. Figure 6 shows an example of tracking results of the straight-line, circular, and "8"- shape (with radius 6 m) trajectories at $v_r = 2.1$ m/s. As shown in Fig. 6(a), the position tracking errors are less than 0.15 m for the straight-line tracking. For both the circular (Fig. 6(b)) and "8"-shape (Fig. 6(c)) trajectory tracking, the position errors are less than 0.8 m. Figures 6(d)–6(f)

show the roll angle tracking results of these three trajectories. The roll angle errors for the straight-line tracking control are plotted over the horizontal position, while for circular and "8"-shape trajectories, they are plotted over the arc-length. It is clear that roll motion followed the calculated BEM closely.

We computed the mean and standard deviation values of the tracking errors under different trajectories and velocities setups. Under each set of those conditions, we repeated four testing runs similar to those shown in Fig. 6 to calculate the statistics. Figure 7 shows the calculated means and standard deviations of the tracking errors (i.e., $\|\boldsymbol{e}_p\| - |e_{\varphi_b}|$). Under the same velocity, the straight-line tracking always has the smallest position errors and roll angle errors, while the errors under the circular tracking are smaller than those under the "8"-shape trajectory. The roll angle reference (i.e., BEM) displays a sudden change when the robot turning direction changes; see Figs. 6(c) and 6(f). This motion requirement can bring a larger tracking error for the "8"-shape trajectory than the circular trajectory. It is clear that the tracking errors for the large-radius trajectory are smaller than those of the small-radius trajectory. With large velocity, both the position and roll motion errors increase. The position tracking error and roll motion error are related to each other, that is, both errors change in the same trend under velocity and trajectory radius variations.

We further implemented controllers $\mathcal{C}$ and $\overline{\mathcal{C}}$ for straight-line and circular trajectories. Figures 8(a) and 8(b) show the position trajectory and the tracking errors, respectively. Figure 8(c) shows the roll angle profiles. Under both controllers, the bikebot successfully followed the straight line. Under $\overline{\mathcal{C}}$, the bikebot reached the desired trajectory in a smoother fashion and with smaller errors than those under $\mathcal{C}$. This is clearly reflected by the control inputs in Figs. 8(e) and 8(d). Without using the gyrobalancer, after crossing the desired trajectory, the bikebot continued to turn (at 86 s in Fig. 8(d)). In contrast, the gyrobalancer helped to generate additional torques to assist balance tasks (e.g., at $t = 103$ s in Fig. 8(e)). Figure 9 shows the results for tracking a circular trajectory. Compared with trajectory under $\overline{\mathcal{C}}$ in Fig. 9(a), a larger steering effect is shown in Fig. 9(b) right after the bikebot entered the circular trajectory (around $t = 82$ s). This sharp turn is also observed
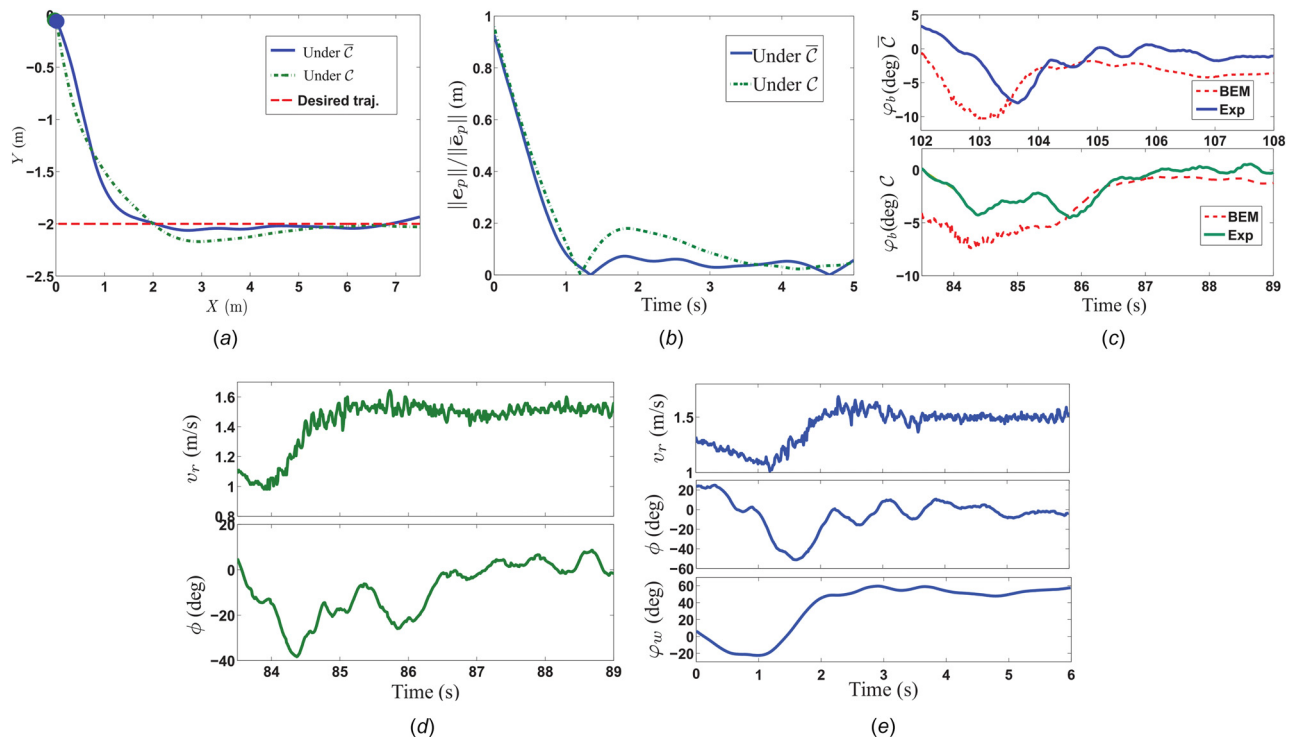


**Fig. 8 Performance comparison of the two controllers $\mathcal{C}$ and $\overline{\mathcal{C}}$ for a straight-line trajectory: (a) The position trajectories in the X–Y plane, (b) position tracking errors, (c) bikebot roll angles under $\mathcal{C}$ and $\overline{\mathcal{C}}$, (d) control inputs under $\mathcal{C}$, and (e) control inputs under $\overline{\mathcal{C}}$**
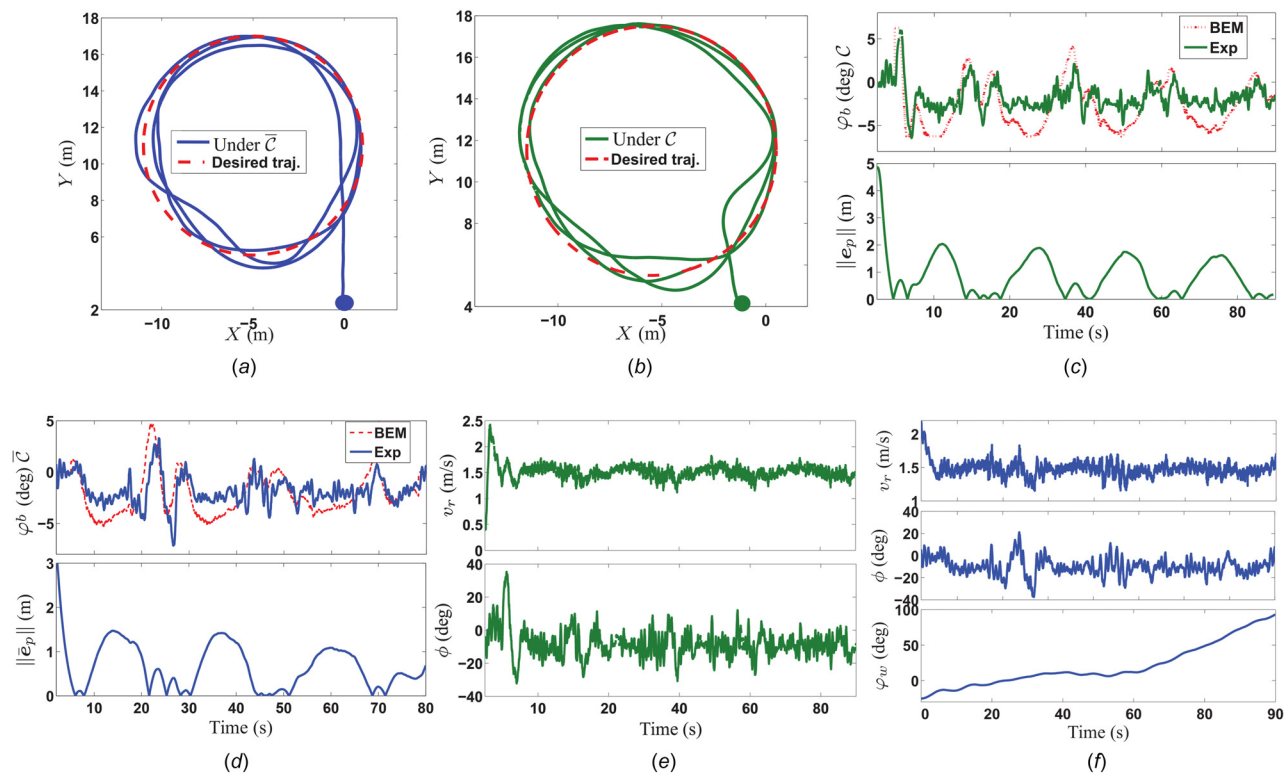
**Fig. 9** Performance comparison of $\mathcal{C}$ and $\bar{\mathcal{C}}$ for a circular trajectory: (*a*) The trajectory under $\bar{\mathcal{C}}$, (*b*) the trajectory under $\mathcal{C}$. The solid circular dots indicate the starting locations, (*c*) position tracking errors and roll angle under $\mathcal{C}$, (*d*) position tracking errors and roll angle under $\bar{\mathcal{C}}$, and (*e*) and (*f*) control inputs under $\bar{\mathcal{C}}$ and $\mathcal{C}$, respectively.

from the roll angle in Fig. 9(*c*). The steering effort to balance the platform was reduced and smoothed by the gyrobalancer. The magnitude of tracking error $\|\bar{e}_p\|$ (Fig. 9(*d*)) is smaller than $\|e_p\|$ (Fig. 9(*c*)). The control inputs under $\bar{\mathcal{C}}$ and $\mathcal{C}$ are illustrated in Figs. 9(*e*) and 9(*f*), respectively.

We now demonstrate the stationary balance results. Figure 10 shows the phase portraits of the bikebot roll angle (Fig. 10(*a*)) and the pivoting angle (Fig. 10(*b*)) when the bikebot was stationary. The bikebot was released at $\varphi_b(0) = -1.2$ deg and $\dot{\varphi}_b(0) = 0$ deg/s with $\varphi_w(0) = 0$ deg. From the figure, the desired roll angle orbit reached $\pm 2$ deg and roll angular rate to $\pm 5$ deg/s. From Fig. 10(*a*), after several periods, the bikebot roll angle was controlled to near the desired rolling orbit around $\pm 2$ deg. Once the roll motion reached the desired orbit, the flywheel pivoting motion was also near the pivoting orbit within the range of $\pm 50$ deg as shown in Fig. 10(*b*).

Figure 11 shows the results under the stationary-moving switch control. The bikebot was controlled from stationary to moving and back to stationary again to track a straight-line trajectory. As shown in the figure, the stationary stages were from $t = 66.2$ to $81.6$ s and from $t = 104.7$ to $118.5$ s. The switching velocities were set as $v_1^* = 1.2$ m/s and $v_2^* = 1.9$ m/s. Figures 11(*a*) and 11(*b*) show the roll angle $\varphi_b$, velocity $v_r$, and steering angle $\phi$ and flywheel pivoting angle $\varphi_w$, respectively. Figure 11(*c*) shows the bikebot planar position, and the position errors are held within 0.4 m. The bikebot was first released at a small $\varphi_b$, and under the gyrobalancer orbital regulation control, the roll motion was within the range of $\pm 1$ deg. After $v_r > v_1^*$, the bikebot moved around $v_r = 2$ m/s, and $\varphi_w$ was set to zero, and the platform was stabilized by steering control. From $t = 104.7$ s (i.e., $v_r < v_2^*$), the bikebot moved into the stationary phase under the gyrobalancer control. After a 5 s transition duration, the roll angle followed a periodical motion, and the steering angle was set to zero.

We further compare the autonomous control results with human riding experiments. The results under controller $\mathcal{C}$ (i.e., without using the gyrobalancer) are compared with these under the human steering control. Figure 12 shows comparison results of tracking an

"8"-shape trajectory (radius of 6 m) with velocity $v_r = 2.1$ m/s. From Fig. 12(*a*), the control performance under the human rider and the autonomous control is in general similar though the former maintains smaller tracking errors than the latter. Figure 12(*b*) shows the steering and roll angles under the two types of controllers. It is clear that under autonomous control, the roll motion experienced less oscillation than that under the rider control. The high-frequent steering actuation by the rider might result in small position errors. Figure 13(*a*) further shows the position comparison of tracking a smaller "8"-shape trajectory (with a radius of 3 m). The motion velocity was selected at a value under which emergency protection can be provided by a human operator immediately to avoid any damage in experiments. Figure 13(*b*) shows the comparison of velocity and the steering angle profiles under the human riding and controller $\mathcal{C}$. In this case, the tracking errors under $\mathcal{C}$ are in general smaller than those under human control. The human balance motor control might be similar to those under $\mathcal{C}$. This observation can be found in the velocity and steering angle comparison plots in Figs. 13(*b*) and 13(*c*). The overall velocity and steering actuation trends under human control and $\mathcal{C}$ are also similar. Indeed, the results in Ref. [32] have shown that the EIC-based control by Eq. (10) has the same mathematical structure as the human neuro-controller that was empirically built on the human riding experiments.

**4.3 Discussion.** In this work, the planar motion of the bikebot is built on the kinematics model (with the nonholonomic constraint), while the roll motion is based on the dynamics model. This paper mainly extends the EIC-based trajectory tracking and balance control of autonomous bikebots with given desired trajectories. The motion control only uses the steering and velocity actuation as the basic design. With an additional gyrobalancer assistive device, the motion is extended to include the stationary balance. The influence of the steering on bikebot dynamics was developed through the balance torque as explained in Ref. [33]. A similar model has been used to analyze and demonstrate that bikebot riders
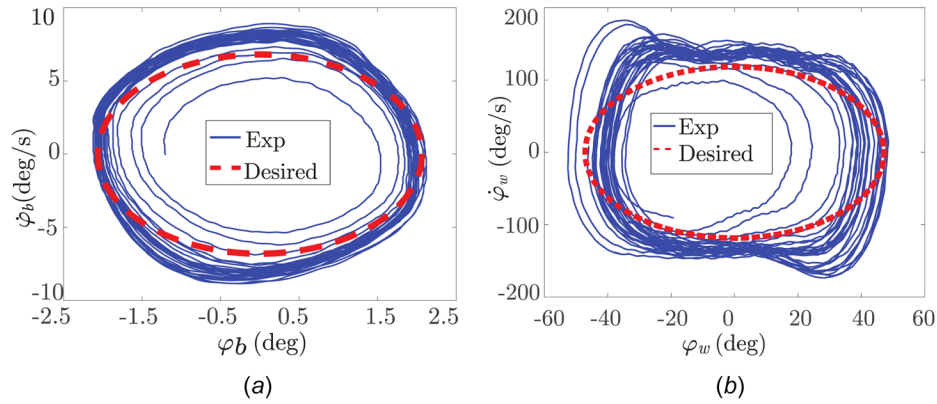
**Fig. 10 Gyrobalancer orbital regulation results: (a) Rolling motion on the $\varphi_b$–$\dot\varphi_b$ plane and (b) flywheel pivoting motion on the $\varphi_w$–$\dot\varphi_w$ plane**
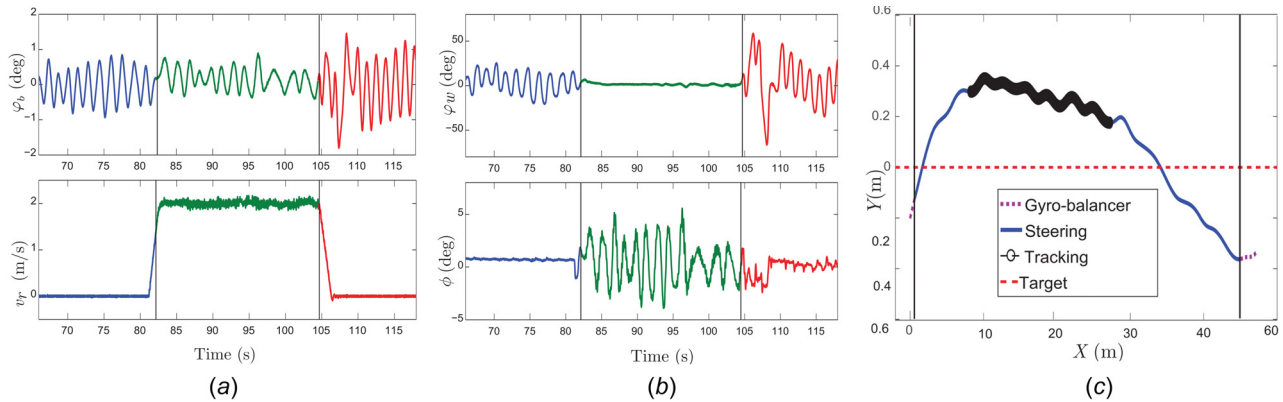


**Fig. 11 Switching balancing control result: (a) bikebot roll angle $\varphi_b$ and velocity $v_r$ and (b) gyropivoting angle $\varphi_w$ and steering angle $\phi$. The first and the third sections are for the gyro balancer control, and the middle section is for the steering balancing control. (c) Bikebot trajectory on $XY$ plane. The vertical lines indicate the time when the control actuation is switched.**

would prefer to use steering actuation than the upper-body leaning motion to overcome any perturbations [26]. For most experimental examples in this work, the bikebot speeds were mild (e.g., 1–3 m/s), and the steering-induced balance torque was not significant compared with these in the high-speed cases.

As we explained previously, the work in Refs. [12] and [13] considered a dynamic model for the motorcycle planar motion, and tire-road interactions are among the important part of the model for aggressive velocity planning. Compared to the dynamic model for planar motion, the kinematic model used in this paper is simple and maintains critical properties such as nonholonomic constraints for relatively mild velocity navigation. The trajectory planning and aggressive maneuvers are not among the main design goals of this work. This is the main difference with the work in Ref. [12]. In order to plan the motion trajectory and maximum velocity profile, we do

need to know the tire-road interactions properties (e.g., friction circles, etc.) This would bring complex dynamic model for the bikebot planar motion, such as those in Refs. [12–14]. It would be helpful to incorporate the motion planning as part of an extension for future development.

Following the above discussion, the existence of the BEM by Eq. (9) is based on the assumption that the bikebot roll motion can be realized. That implies that the algebraic equation $F(q, u^{\text{ext}}, \tau) = B(q)u^{\text{ext}} + \tau - C(q, 0) - G(q) = 0$ has a feasible solution that satisfies the roll motion dynamics under given $u^{\text{ext}}$ and $\tau$. The solution of this equation depends on the external controller $u^{\text{ext}}$. If for a given trajectory, such as a sharp turn, under the designed $u^{\text{ext}}$, there is no feasible roll motion and then a revised trajectory-tracking controller or replanning the trajectory is needed. Since the demonstrated experiments took smooth trajectories and reasonable
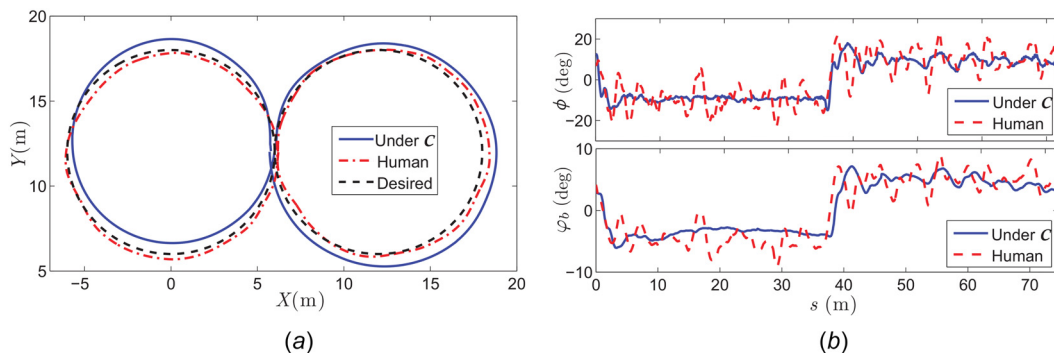


**Fig. 12 Path following ("8"-shape trajectory) comparison of the bikebot control and rider experiments: (a) horizontal position and (b) steering angle $\phi$ and rolling angle $\varphi_b$**
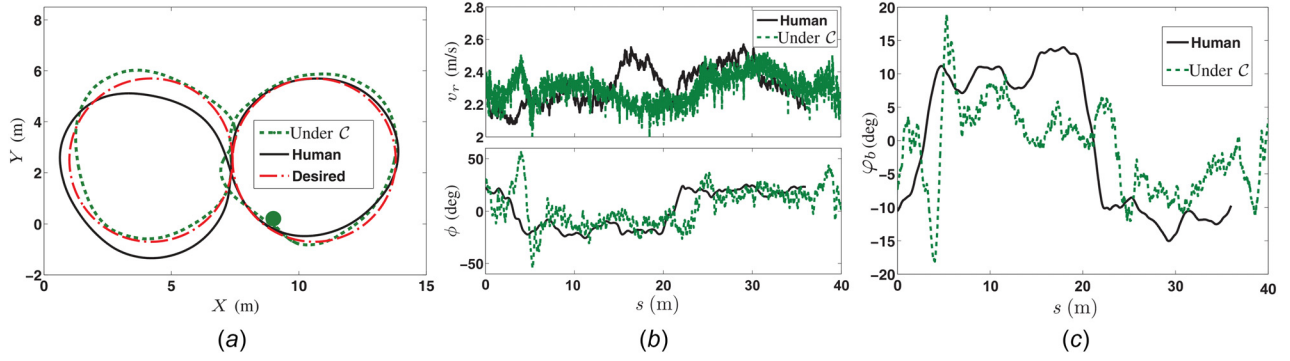
**Fig. 13** Performance comparison of human riding and the controller $\mathcal{C}$ to follow an "8"-shape trajectory: (*a*) The tracking trajectory under a human riding control. The solid circular dot indicates the starting location. (*b*) Controller inputs under human control and $\mathcal{C}$. (*c*) Balancing roll angles.

velocity profiles, the control design always found the equilibrium solution of Eq. (9). For a given desired trajectory, we can also design a path-following controller, instead of trajectory tracking control as shown in this paper, by taking a time suspension technique to tune the bikebot velocity with the path-following errors [34]. This approach would help design a feasible velocity profile to follow a given path for the bikebot control.

## 5 Conclusion

We presented a set of gyroscopic balancer-enhanced control strategies for the autonomous bikebot for simultaneous trajectory tracking and platform balance. The control design was built on the EIC structure of the bikebot dynamics. The balance equilibrium manifold played a critical role to build the interconnection of the trajectory tracking and the balance roll motion profiles. When the platform was stationary, the gyrobalancer mainly provided the balancing torque. A switching strategy between the velocity and steering control laws was proposed to interconnect to the trajectory tracking controller. We presented extensive experiments to validate and demonstrate the autonomous control performance and also compared them with the human riding experiments. It was confirmed that the human riding and autonomous control strategies shared a similar steering and velocity actuation for tracking trajectory and maintaining balance. As an ongoing future work direction, incorporating the bikebot dynamics model and tire-road interactions into the trajectory planning would help design motion controllers for high-performance agile maneuvers.

## Appendix A: Proof of Lemma 1

From Eqs. (19) and (20), this lemma is equivalent to prove $|\bar{d}_0| \leq |d_0|$. For the case of $|d_0| < \varepsilon_d$, we have $u_w^0 = 0$, thus $|\bar{d}_0| = |d_0|$. Therefore $||\bar{\boldsymbol{d}}_p|| = ||\boldsymbol{d}_p||$. For the case $|\bar{d}_0| > \varepsilon_d$, we have

$$d_0 - \bar{d}_0 = u_\psi^{\text{int}} - \bar{u}_\psi^{\text{int}} = g_\psi^{-1}(\varphi_b) g_w(\varphi_b) u_w \qquad (A1)$$

From the sign and amplitude definition of $u_w$, we conclude the following relationships: $\text{sign}(d_0) = \text{sign}\left(g_\psi^{-1}(\varphi_b) g_w(\varphi_b) u_w\right)$ and $|g_\psi^{-1}(\varphi_b) g_w(\varphi_b) u_w| \leq |d_0| - \varepsilon_d < |d_0|$. Thus, we take the absolute value of Eq. (A1) without changing the form and obtain $|d_0| - |\bar{d}_0| = |g_\psi^{-1}(\varphi_b) g_w(\varphi_b) u_w| > 0$. This completes the proof.

## Appendix B: Proof of Theorem 1

We prove the result through the Lyapunov stability theorem [35]. Using variable $\boldsymbol{e}_x = \left[\boldsymbol{e}_p^T \; \dot{\boldsymbol{e}}_p^T \; \ddot{\boldsymbol{e}}_p^T\right]^T$, we rewrite the error dynamics by Eq. (17) as

$$\dot{\boldsymbol{e}}_x = \boldsymbol{A}\boldsymbol{e}_x + \boldsymbol{d}_p$$

with $\boldsymbol{A} = \boldsymbol{A}_0 \otimes \boldsymbol{I}_2$, where operator $\otimes$ represents the Kronecker product, $\boldsymbol{I}_n$ is the $n \times n$ identity matrix, and

$$\boldsymbol{A}_0 = \begin{bmatrix} \boldsymbol{0} & \boldsymbol{I}_2 \\ -b_0 & \boldsymbol{b} \end{bmatrix}, \quad \boldsymbol{b} = \begin{bmatrix} -b_1 & -b_2 \end{bmatrix}$$

We consider the Lyapunov candidate function $V = \boldsymbol{e}_x^T \boldsymbol{P} \boldsymbol{e}_x$, where positive matrix $\boldsymbol{P} = \boldsymbol{P}^T \in \mathbb{R}^{6 \times 6}$ satisfying $\boldsymbol{A}^T \boldsymbol{P} + \boldsymbol{P} \boldsymbol{A} = -\boldsymbol{I}_6$. Following the stability of the perturbed systems [35] and Eq. (26), we obtain

$$\dot{V} \leq -\left(\frac{1}{\lambda_2} - k_1 \frac{2\lambda_2}{\lambda_1}\right) V + 2\lambda_2 k_0 \sqrt{\frac{V}{\lambda_1}} \qquad (B1)$$

where $\lambda_1, \lambda_2 > 0$ are the minimum and maximum eigenvalues of $\boldsymbol{P}$, respectively. Defining $W = \sqrt{V}$, we write Eq. (B1) as

$$\dot{W} \leq -\upsilon W + \frac{2\lambda_2 k_0}{\sqrt{\lambda_1}} \qquad (B2)$$

where $\upsilon = \frac{1}{2}\left(\frac{1}{\lambda_2} - k_1 \frac{2\lambda_2}{\lambda_1}\right) > 0$, namely, $k_1 < \frac{\lambda_1}{2\lambda_2^2}$. Considering $W(t) = \sqrt{V(t)} \geq \sqrt{\lambda_1} ||\boldsymbol{e}_x(t)||$ and by comparison lemma [35], from Eq. (B2), we obtain

$$||\boldsymbol{e}_x(t)|| \leq \lambda_r e^{-\upsilon t} ||\boldsymbol{e}(0)|| + \frac{2\lambda_r^2 k_0}{\upsilon} =: e_p^b(t) \qquad (B3)$$

where $\lambda_r = \lambda_2 / \lambda_1$. Similarly, for the error dynamics under controller $\bar{\mathcal{C}}$, we obtain

$$||\bar{\boldsymbol{e}}_x(t)|| \leq \lambda_r e^{-\bar{\upsilon} t} ||\bar{\boldsymbol{e}}(0)|| + \frac{2\lambda_r^2 \bar{k}_0}{\bar{\upsilon}} =: \bar{e}_p^b(t) \qquad (B4)$$

where $\bar{\upsilon} = \frac{1}{2}\left(\frac{1}{\lambda_2} - \bar{k}_1 \frac{2\lambda_2}{\lambda_1}\right) > 0$ and $\bar{k}_1 < \frac{\lambda_1}{2\lambda_2^2}$. From Eqs. (B3) and (B4), it is straightforward to obtain that both errors exponentially converge to the regions near the origin with bounds $\frac{2\lambda_r^2 k_0}{\upsilon}$ and $\frac{2\lambda_r^2 \bar{k}_0}{\bar{\upsilon}}$, respectively. Given $||\boldsymbol{e}_x(0)|| = ||\bar{\boldsymbol{e}}_x(0)||$ and $\bar{\upsilon} \geq \upsilon$, $e^{-\bar{\upsilon} t} \leq e^{-\upsilon t}$ for any $t$ and $\frac{\bar{k}_0}{\bar{\upsilon}} \leq \frac{k_0}{\upsilon}$, and thus $\bar{e}_p^b(t) \leq e_p^b(t)$ for $t \geq 0$ given $\bar{k}_0 \leq k_0, \bar{k}_1 \leq k_1$. This completes the proof. ∎

## Appendix C: Proof of Lemma 2

We consider the Lyapunov candidate function as

$$V_1(\boldsymbol{x}) = \frac{1}{2}\Delta E^2 + \frac{1}{2}\kappa_1(\xi_3 + L\xi_2)^2$$

Obviously, $V_1(\boldsymbol{x}) \geq 0$. Taking derivative of $V_1$ and using Eq. (31), we obtain

$$\dot{V}_1(\boldsymbol{\xi}) = -m_b h_b \kappa_2 (g + b) v_g^2(\boldsymbol{\xi}) \leq 0$$

By LaSalle theory [35], the system states converge to the invariant set $\mathcal{S}(\boldsymbol{\xi})$ asymptotically. In $\mathcal{S}(\boldsymbol{x})$, $v_g(\boldsymbol{\xi}) = 0$ and then control input $u_g = \frac{Lb}{h_b}\mathsf{s}_{\xi_1}$. Plugging the above $u_g$ into system dynamics in Eq. (29), we obtain that the closed-loop dynamics for $\boldsymbol{\xi}$ are on orbit $\mathcal{O}_b$ and $\mathcal{O}_g$. This completes the proof.

## References

[1] Han, F., and Yi, J., 2021, "Stable Learning-Based Tracking Control of Underactuated Balance Robots," IEEE Robot. Automat. Lett., **6**(2), pp. 1543–1550.
[2] Åström, K. J., Klein, R. E., and Lennartsson, A., 2005, "Bicycle Dynamics and Control," IEEE Control Syst. Mag., **25**(4), pp. 26–47.
[3] Beznos, A., Formal'sky, A., Gurfinkel, E., Jicharev, D., Lensky, A., Savitsky, K., and Tchesalin, L., 1998, "Control of Autonomous Motion of Two-Wheel Bicycle With Gyroscopic Stabilisation," Proceedings of International Conference on Robotics and Automation, Leuven, Belgium, July 6–8, pp. 2670–2675.
[4] Getz, N., 1995, "Dynamic Inversion of Nonlinear Maps With Applications to Nonlinear Control and Robotics," Ph.D. thesis, Department of Electrical Enginnering and Computer Sciences, University of California, Berkeley, CA.
[5] Lee, S., and Ham, W., 2002, "Self-Stabilzing Strategy in Tracking Control of Unmanned Electric Bicycle With Mass Balance," Proceedings of the IEEE/RSJ International Conference on Robots and Systems, Lausanne, Switzerland, Sept. 30–Oct. 4, pp. 2200–2205.
[6] Yi, J., Song, D., Levandowski, A., and Jayasuriya, S., 2006, "Trajectory Tracking and Balance Stabilization Control of Autonomous Motorcycles," Proceedings of International Conference on Robotics and Automation, Orlando, FL, May 15–19, pp. 2583–2589.
[7] Tanaka, Y., and Murakami, T., 2009, "A Study on Straight-Line Tracking and Posture Control in Electric Bicycle," IEEE Trans. Ind. Electron., **56**(1), pp. 159–168.
[8] He, J., Zhao, M., and Stasinopoulos, S., 2015, "Constant-Velocity Steering Control Design for Unmanned Bicycles," Proceedings of IEEE International Conference on Robotics and Biomimetics., Zhuhai, China, Dec. 6–9, pp. 428–433.
[9] Chen, L., Liu, J., Wang, H., Hu, Y., Zheng, X., Ye, M., and Zhang, J., 2021, "Robust Control of Reaction Wheel Bicycle Robot Via Adaptive Integral Terminal Sliding Mode," Nonlinear Dyn., **104**(3), pp. 2291–2302.
[10] Zou, Z., Zhao, R., Wu, Y., Yang, Z., Tian, L., Wu, S., Wang, G., et al., 2020, "A Hybrid and Scalable Brain-Inspired Robotic Platform," Sci. Rep., **10**(1), 18160.
[11] Wang, P., Yi, J., Liu, T., and Zhang, Y., 2017, "Trajectory Tracking and Balance Control of an Autonomous Bikebot," Proceedings of International Conference on Robotics and Automation, Singapore, May 29–June 3, pp. 2414–2419.
[12] Hauser, J., and Saccon, A., 2006, "Motorcycle Modeling for High-Performance Maneuvering," IEEE Control Syst. Mag., **26**(5), pp. 89–105.
[13] Yi, J., Zhang, Y., and Song, D., 2009, "Autonomous Motorcycles for Agile Maneuvers: Part I: Dynamic Modeling," Proceedings of the IEEE Conference on Decision and Control, Shanghai, China, Dec. 15–18, pp. 4613–4618.
[14] Yi, J., Zhang, Y., and Song, D., 2009, "Autonomous Motorcycles for Agile Maneuvers: Part II: Control Systems Design," Proceedings of the IEEE Conference on Decision and Control, Shanghai, China, Dec. 15–18, pp. 4619–4624.
[15] Cerone, V., Andreo, D., Larsson, M., and Regruto, D., 2010, "Stabilization of a Riderless Bicycle: A Linear-Parameter-Varying Approach," IEEE Control Syst. Mag., **30**(5), pp. 23–32.
[16] Zhang, Y., Li, J., Yi, J., and Song, D., 2011, "Balance Control and Analysis of Stationary Riderless Motorcycles," Proceedings of International Conference on Robotics and Automation, Shanghai, China, May 9–13, pp. 3018–3023.
[17] Panzani, G., Todeschini, D., Corno, M., Sette, D., and Savaresi, S. M., 2022, "Co-Design and Experimental Validation of a Gyroscopic Stabilizer for Powered Two-Wheelers," IEEE/ASME Trans. Mechatron., **27**(5), pp. 2484–2494.
[18] Kim, Y., Kim, H., and Lee, J., 2015, "Stable Control of the Bicycle Robot on a Curved Path by Using a Reaction Wheel," J. Mech. Sci. Technol., **29**(5), pp. 2219–2226.
[19] Cui, L., Wang, S., Yang, S., Zhang, Z., and Jiang, Z.-P., 2020, "Nonlinear Balance Control of an Unmanned Bicycle: Design and Experiments," Proceedings of the IEEE/RSJ International Conference on Intelligent Robots and Systems, Las Vegas, NV, Oct. 24, pp. 7279–7284.
[20] Seekhao, P., Tungpimolrut, K., and Parnichkun, M., 2020, "Development and Control of a Bicycle Robot Based on Steering and Pendulum Balancing," Mechatronics, **69**, pp. 102386–12.
[21] Keo, L., and Yamakita, M., 2011, "Control of an Autonomous Electric Bicycle With Both Steering and Balancer Controls," Adv. Robot., **25**(1–2), pp. 1–22.
[22] Hara, S., Nakagami, K., Miyata, K., Tsuchiya, M., and Tsujii, E., 2019, "Dynamics and Control of Self-Standable Motorcycle," ASME Paper No. DETC2019-97154.
[23] Cui, L., Wang, S., Zhang, Z., and Jiang, Z.-P., 2022, "Asymptotic Trajectory Tracking of Autonomous Bicycles Via Backstepping and Optimal Control," IEEE Control Syst. Lett., **6**, pp. 1292–1297.
[24] Shiriaev, A. S., Perram, J. W., and Canudas-de-Wit, C., 2005, "Constructive Tool for Orbital Stabilization of Underactuated Nonlinear Systems: Virtual Constraints Approach," IEEE Trans. Autom. Control, **50**(8), pp. 1164–1176.
[25] Shiriaev, A. S., Freidovich, L. B., Robertsson, A., Johansson, R., and Sandberg, A., 2007, "Virtual-Holonomic-Constraints-Based Design of Stable Oscillations of Furuta Pendulum: Theory and Experiments," IEEE Trans. Rob., **23**(4), pp. 827–832.
[26] Wang, P., and Yi, J., 2016, "Balance Equilibrium Manifold and Control of Rider-Bikebot Systems," Proceedings of the American Control Conference, Boston, MA, July 6–8, pp. 2168–2174.
[27] Wang, P., Yi, J., and Liu, T., 2020, "Stability and Control of a Rider-Bicycle System: Analysis and Experiments," IEEE Trans. Automat. Sci. Eng., **17**(1), pp. 348–360.
[28] Moore, J. K., 2012, "Human Control of a Bicycle,". Ph.D. thesis, Department of Mechanical and Aerospace Engineering, University of California Davis, Davis, CA.
[29] Cain, S. M., 2013, "An Experimental Investigation of Human/Bicycle Dynamics and Rider Skill in Children and Adults," Ph.D. thesis, Department of Biomedical Engineering, University of Michigan, Ann Arbor, MI.
[30] Wang, P., Gong, Y., Yi, J., and Liu, T., 2019, "An Integrated Stationary/Moving Balance Control of an Autonomous Bikebot," American Control Conference (ACC), Philadelphia, PA, July 10–12, pp. 3273–3278.
[31] Zhang, Y., Wang, P., Yi, J., Song, D., and Liu, T., 2014, "Stationary Balance Control of a Bikebot," Proceedings of International Conference on Robotics and Automation, Hong Kong, China, May 31–June 7, pp. 6706–6711.
[32] Wang, P., and Yi, J., 2015, "Dynamic Stability of a Rider-Bicycle System: Analysis and Experiments," Proceedings of the American Control Conference, Chicago, IL, July 1–3, pp. 1161–1166.
[33] Fajans, J., 2000, "Steering in Bicycles and Motorcycles," Am. J. Phys., **68**(7), pp. 654–659.
[34] Zhang, Y., and Yi, J., 2010, "Velocity Field-Based Maneuver Regulation of Autonomous Motorcycles," Proceedings of IFAC Symposium on Mechatronic Systems, Cambridge, MA, Sept 13–15, pp. 385–392.
[35] Khalil, H. K., 2002, Nonlinear Systems, 3rd ed., Prentice Hall, Upper Saddle River, NJ.